

# Experimental protection of qubit coherence by using a phase-tunable image drive

S. Bertaina,<sup>1,\*</sup> H. Vezin,<sup>2</sup> and I. Chiorescu<sup>3,†</sup>

<sup>1</sup>CNRS, Aix-Marseille Université, IM2NP (UMR 7334), Institut Matériaux  
Microélectronique et Nanosciences de Provence, Marseille, France.

<sup>2</sup>CNRS, Université de Lille, LASIR (UMR 8516), Laboratoire de Spectrochimie Infrarouge et Raman, Villeneuve d'Ascq, France

<sup>3</sup>Department of Physics, The National High Magnetic Field  
Laboratory, Florida State University, Tallahassee, Florida 32310, USA.

The protection of qubit coherence is an essential task in order to build a practical quantum computer able to manipulate, store and read quantum information with a high degree of fidelity. As open quantum systems, coherence in spin qubits is limited by spin-spin interactions, spin diffusion, inhomogeneity of the static and microwave fields<sup>1</sup> as well as charge noise<sup>2</sup>. An increase in coherence time is achieved by dynamically decoupling (DD) qubits from their surroundings using distinct Electron Spin Resonance (ESR) pulses<sup>3,4</sup>. However, such pulses have inherent imperfections and fluctuations, thus requiring their own layer of DD, resulting in a doubly dressed qubit. The technique of concatenated DD<sup>5</sup> has been successfully applied to NV centers up to the second order of dressing<sup>5-8</sup>. Here, we demonstrate a pulse protocol based on Floquet modes which successfully increases the decoherence time in a number of materials with different spin Hamiltonians and environments, such as low and high spin-orbit coupling for instance. For spin relaxation times accessible to our measurement setup (at around 40 K) one can do a direct comparison with the coherence time, and we demonstrate the regime  $T_2 \approx T_1$ .

The use of strong continuous microwave excitation has been proposed as a way to protect qubits<sup>9,10</sup> although the quantum gates would need proper redesigning. In related studies, complex pulse design using an arbitrary waveform generator, proved essential in studying Floquet Raman transitions<sup>11,12</sup> and quantum metric of a two-level system<sup>13</sup> in NV centers. It is worth noting that in the case of concatenated DD, the frequency of the second order ( $n = 2$ ) excitation has to match the Rabi frequency of the first excitation ( $n = 1$ ); also, the two excitations are linearly polarized and perpendicular to each other (the method extends to higher orders in  $n$ ). Experimentally, the protocol quickly becomes complex and demanding in terms of pulse design and frequency stability, above the second order.

Our protocol uses two coherent microwave pulses: a main pulse drives the qubit Rabi precession while a low-power, circularly polarized (image) pulse continuously sustains the spin motion. The image drive has a frequency close to the main drive and thus presents less technical challenges compared to the concatenated protocol. Moreover, its initial phase allows to tune the spin dynamics by enhancing (or diminishing) the Floquet modes<sup>14</sup> of its second dressing. The technical implementation is simple and can be generalized to any type of qubit, such as superconducting circuits or spin systems.

The standard method to induce Rabi oscillations in a two-level system (TLS) is to apply an electro-magnetic pulse of frequency  $f_0$  equal to the TLS level separation (resonance regime). The pulse will drive the spin population coherently between the two states. Experimentally, the drive is at a frequency  $f_0 + \Delta$  (where  $f_0$  is the Larmor frequency and  $\Delta$  is a small detuning away from the resonance condition) followed by read out pulses of frequency  $f_0$  to record the state  $\langle S_z \rangle$  (see Fig. 1a). The method introduced here makes use of two coherent microwave pulses (see Fig. 1b,c): the drive at  $f_0 + \Delta$  creates quantum Rabi oscillations while the second one sustains them using a very low power image of the drive, operated at  $f_0 - \Delta$ . Fig. 1b shows one way of coherently creating the drive and its image, by means of a mixer multiplying a pulse at frequency  $f_0$  with an intermediate frequency (IF) cosine signal allowing to control the detuning  $\Delta$ , phase  $\phi$  and the pulse length, shape and amplitude. Technical details are presented in the *Supplementary Information, Sect. III*.

Rabi oscillations of three different types of paramagnetic systems – a rare earth ion ( $\text{Gd}^{3+}$ ), a transition metal ion ( $\text{Mn}^{2+}$ ) and a defect in diamond (P1) – are shown in Fig. 1 (d,e,f), respectively. Their detuned Rabi oscillations induced by the drive pulse only (red curves) are of similar frequency ( $\approx 20$  MHz) and last for a small number of nutations ( $< 20$ ). The blue curve shows the Rabi oscillation when the image pulse is simultaneously applied to the spin systems. The oscillations remain intense far beyond the decay time of the red curves and their number is dramatically increased. This effect has maximum impact when the frequency difference between the drive and the image pulses  $2\Delta$  matches the Rabi frequency induced by the main drive,  $F_R$ . In addition of the very long coherence time, we observe a slow amplitude modulation, sensitive to the phase  $\phi$  and attributed to Floquet modes, as explained below.

We study the new physical limitation of the Rabi oscillation under image pumping condition, by tuning the relaxation time via temperature control and by applying the longest drive pulse available to us (Fig. 2). The drive limitation is due to the pulse power amplifier of the setup, with a maximum pulse length of  $15 \mu\text{s}$ . At 40 K, the relaxation time of the spin system  $\text{MgO}:\text{Mn}^{2+}$  ( $S = 5/2$ ) is also  $\approx 15 \mu\text{s}$ . The Rabi oscillation for the transition  $+\frac{1}{2} \leftrightarrow -\frac{1}{2}$  is shown in Fig. 2. Guidelines showing the exponential decays due to  $T_2$  (in green) and  $T_1$  (in orange) measured by Hahn echo and inversion recovery

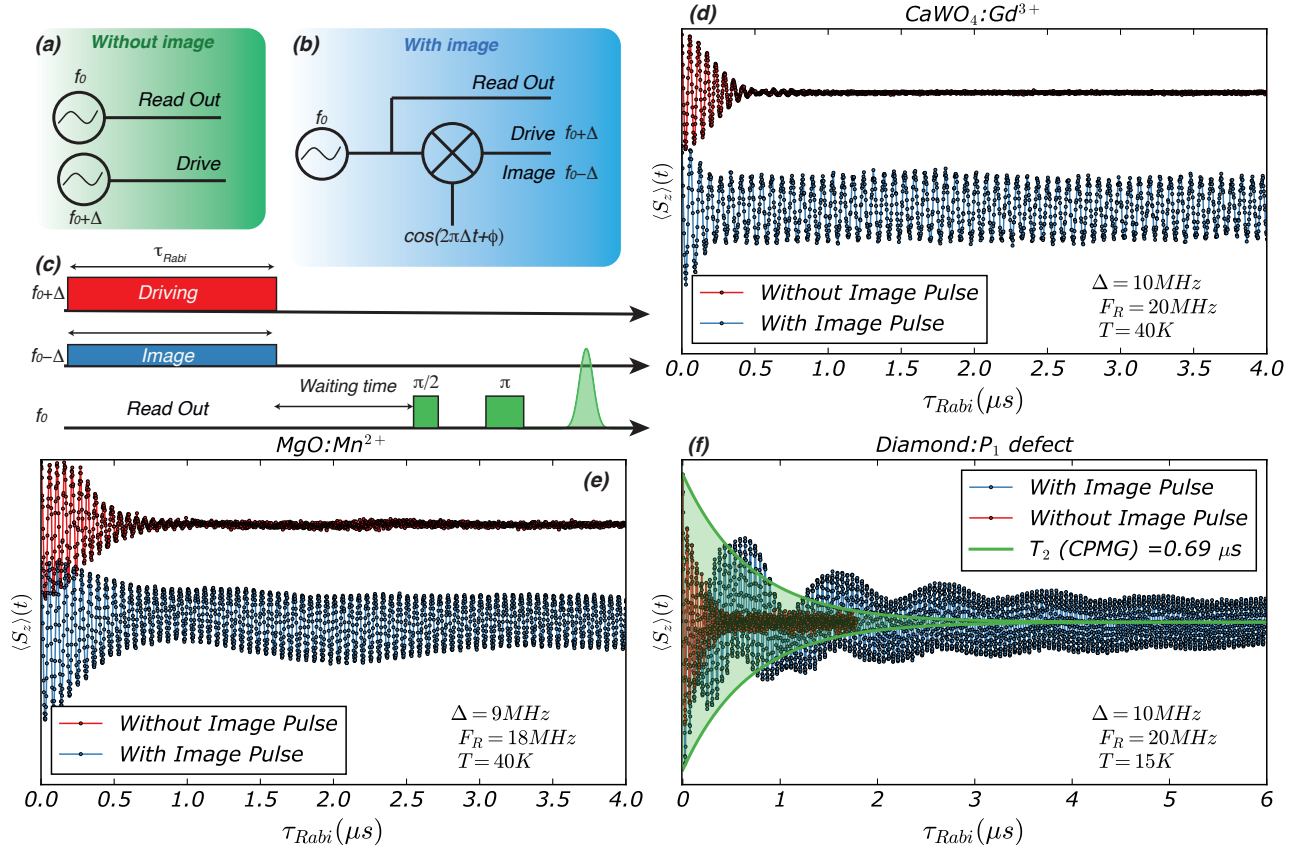


Figure 1. **Comparison of Rabi oscillation with or without the image pulse.** **a,b,c**, Schematic of the microwave implementation. **a**, The drive ( $f + \Delta$ ) and the readout ( $f_0$ ) sources are independent. **b**, Using the same source as the readout ( $f_0$ ), the drive pulse ( $f_0 + \Delta$ ) is generated by a non-linear mixing with a low frequency signal  $\Delta$ , with  $f_0/\Delta \sim 10^3$ , process that creates a low-amplitude image drive ( $f_0 - \Delta$ ) as well. The drive, image and readout pulses are coherent and the phase relationship is tunable. **c** Pulse sequence (see *Methods*): the drive and the image pulses act at the same time on the qubit while the readout is sensitive to the  $S_z$  projection by a spin-echo process. **d,e,f** Rabi oscillation of the  $\text{CaWO}_4:\text{Gd}^{3+}$ ,  $\text{MgO}:\text{Mn}^{2+}$  and P1 defects respectively in the presence (blue) or absence (red) of the image pulse at the optimum condition  $F_R = 2\Delta$ . The green guideline in **f** shows the improvement of the coherence time when compared to a CPMG pulse sequence while the blue curve shows not only a long coherence but also beatings which are tunable via phase-tunable Floquet dynamics (see text).

respectively, are added as well. While the amplitude of the Floquet mode (slow amplitude modulation) decreases with  $T_2$ , the Rabi oscillations persists with a decay time equal to  $T_1$ . In magnetic diluted systems,  $T_1$  is usually much bigger than  $T_2$ . Recently it has been shown in Si:Bi that  $T_1$  can be tuned and reach thousand of seconds<sup>15</sup>. The method presented here can lead to very long persistent Rabi oscillations, using a single circularly polarized image pulse.

To understand how the coherence protection mechanism is created, we start with the spin Hamiltonian in the laboratory frame (see *Methods* and the *Supplementary Information*, Sect. III) :

$$\mathcal{H} = f_0 S_z + 2h_d S_x \sin(\omega_+ t + \phi) + 2h_i S_x \sin(\omega_- t - \phi - \theta) \quad (1)$$

where  $f_0$  is the Larmor frequency caused by the static field,  $h_d$  and  $h_i$  are the microwave drive and image field, respectively,  $\frac{\omega_{\pm}}{2\pi} = f_0 \pm \Delta$ ,  $\phi$  is a tunable phase (see

Fig. 1) and  $\theta$  is a small additional phase, potentially created by imperfections of the setup (as discussed in *Supplementary Information*). Variables  $f_0, h_{d,i}$  and  $\Delta$  are expressed in units of MHz. After a transformation in a frame rotating with  $\omega_+$ , the Hamiltonian (1) becomes :

$$\mathcal{H}_{RF} = -\Delta S_z + h_d (S_x \sin \phi - S_y \cos \phi) - h_i [S_x \sin(4\pi\Delta t + \phi + \theta) + S_y \cos(4\pi\Delta t + \phi + \theta)]. \quad (2)$$

When the image field  $h_i$  is absent, the equation (2) has no explicit time dependence and the Rabi frequency is simply  $F_R = \sqrt{\Delta^2 + h_d^2}$ . When  $h_i$  is present, the dynamics of  $\langle S_z \rangle$  can be solved numerically, as it is shown in Fig. 3 for the case of  $\text{CaWO}_4:\text{Gd}^{3+}$ .

For a fixed power  $h_d$  of the drive pulse, Rabi oscillations are measured as a function of the detuning  $\Delta$ . As shown in the contour plot of Fig. 3a,  $\langle S_z \rangle(t)$  vanishes after few oscillations except when the condition  $F_R \sim 2\Delta$  is met. At this Floquet resonance,  $\langle S_z \rangle$  keeps oscillating

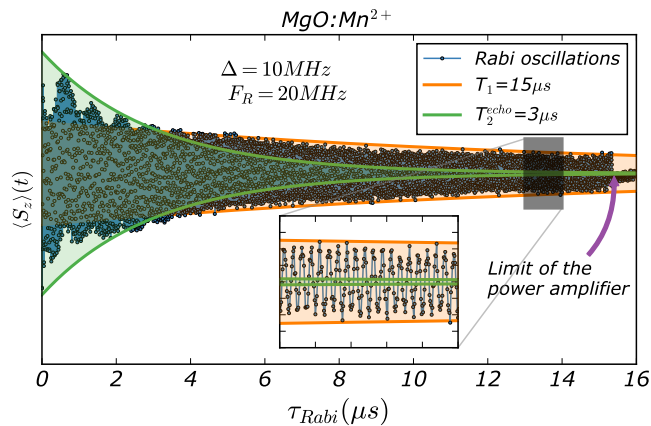


Figure 2. **Rabi decay under image pumping condition at 40 K.** The decay of the Rabi oscillations (green) for a  $\text{Mn}^{2+}$  spin is limited by the relaxation time  $T_1$  (orange) when an image pulse is used to sustain the dynamics. The inset shows the long-lived oscillations, all the way up to the 15  $\mu\text{s}$  limit as imposed by the power amplifier of the setup.

for a very long time ( $> 15 \mu\text{s}$ ). Its Fast Fourier Transform (FFT) is presented in Fig. 3b. The free (unprotected) Rabi oscillations mode  $F_R$  is rather weak and broad showing the large damping caused by the environment. However, when the mode crosses the frequency of the image pulse, indicated by the vertical white dashed line, the peak becomes more intense and narrower, as the qubit protection from environment is activated. The condition  $F_R = \sqrt{\Delta^2 + h_d^2} = 2\Delta$  (or  $h_d = \sqrt{3}\Delta$ ) correspond to the most efficient protection of the Rabi oscillation (see *Supplementary Information, Sect. III*). We can compare the experimental result to the model described by the Hamiltonian (2). Figure 3c shows the FFT of  $\langle S_z \rangle(t)$  computed using the time evolution of  $\mathcal{H}_{RF}$ . Input parameters such as  $h_d$ ,  $h_i$  as well as  $T_2$  are experimental values obtained from independent measurements (see *Methods*). The Hamiltonian (2) describes very well the protection of the coherence by means of the image pulse. Note the existence of a Floquet mode at  $\Delta = 7.5 \text{ MHz}$  of frequency  $\sim 1 \text{ MHz}$ , visible in both the experimental and theoretical contour plots of Fig. 3.

The Floquet mode appears as beatings of the Rabi frequency and is  $\phi$ -tunable. Similarly to the case of  $\text{Gd}^{3+}$ , the qubit protection and Floquet mode dynamics is obtained for the  $S = 5/2$  spin of  $\text{MgO}:\text{Mn}^{2+}$ , here measured in the experimental conditions of Fig. 2. Rabi oscillations and corresponding FFT spectra are shown in Fig. 4 for two values of the initial phase,  $\phi = 0^\circ$  (green) and  $\phi = 45^\circ$  (gold), while simulations are shown in black. The decay times are much exceeding  $T_2$  for both values (here  $T_1 \approx 15 \mu\text{s}$ , see Fig. 2); however, the dynamics is strikingly different. When the drive and image pulses have the same initial phase (one can consider the initial time in Eq. 2 as  $-\frac{\theta}{4\pi\Delta}$  without loss of generality), the Rabi oscillations have maximum visibility, with no

beatings. At  $\phi = 45^\circ$ , the spin torques generated by the  $h_d$  and  $h_i$  fields induce strong beatings or a Floquet mode creating two additional modes of the Rabi frequency. The left panel shows Rabi splittings equal to the Floquet frequency for  $\phi = 45^\circ$  and a single Rabi oscillation for  $\phi = 0^\circ$ .

Experimentally, we can continuously vary the value of  $\phi$  and analyze the frequency and intensity of the Floquet mode. As an example, a comparison between theory and experiment is shown in Fig. 5 for the case of  $\text{CaWO}_4:\text{Gd}^{3+}$  for  $\Delta = h_d/\sqrt{3} = 34 \text{ MHz}$ . For even and odd multiples of  $\pi/4$ , a single and a splitted Rabi mode is observed, respectively. The Rabi splitting is the Floquet mode and is constant as a function of  $\phi$ . However, its intensity oscillates with a period of  $\pi/2$  as imposed by the geometry of the  $h_{d,i}$  torques on the qubit: when aligned ( $\parallel$  or  $\text{anti-}\parallel$ ) no beatings are present and the Rabi oscillation is optimally sustained; when perpendicular, the beatings are maximized generating a visible Floquet mode. The effect is evident in simulations as well, since the terms in  $h_{d,i}$  of  $\mathcal{H}_{RF}$  are along the same direction or orthogonal, for  $\phi = 0^\circ$  and  $45^\circ$  respectively.

The qubit rotation in spin space is thus tunable by using a pre-selected value of  $\phi$ , allowing to create complex pulsed rotations. With a decoherence time approaching spin lifetime  $T_1$ , the value of  $\phi$  can be changed while qubit control is still ongoing. Our study demonstrates a sustained qubit coherence ( $T_2 \approx T_1$ ) using a general protocol that can be readily implemented to any type of qubit. Similarly, our approach can be used in many detection schemes, such as sensitive spin detection using on-chip resonance techniques<sup>16–18</sup>.

*Acknowledgements.* ESR measurements were supported by the CNRS research infrastructure RENARD (award number IR-RPE CNRS 3443). Partial support by the National Science Foundation Cooperative Agreement No. DMR-1644779 and the State of Florida is acknowledged.

## METHODS

*Spectrometer setup.* The measurements have been performed on a conventional pulse ESR spectrometer Bruker E680 equipped with an incoherent electron double resonance (ELDOR) bridge and a coherent arbitrary waveform generator (AWG) bridge. In the ELDOR bridge (Fig. 1a), the drive and the read out pulses come from two independent sources while with the AWG bridge (Fig. 1b) all the pulses are generated using the same microwave source and thus they are all phase coherent. The drive frequency is generated by mixing the source  $f_0$  (used as a local oscillator) with a low frequency and phase controllable signal  $IF(\Delta, \phi)$  through an in-phase quadrature (IQ) mixer. Ideally, the output of the mixer is monochromatic with the frequency  $f_0 + \Delta$ . In reality, the output consists of a principal frequency  $f_0 + \Delta$  (the drive) and of lower amplitude images  $f_0 + n\Delta$  (see

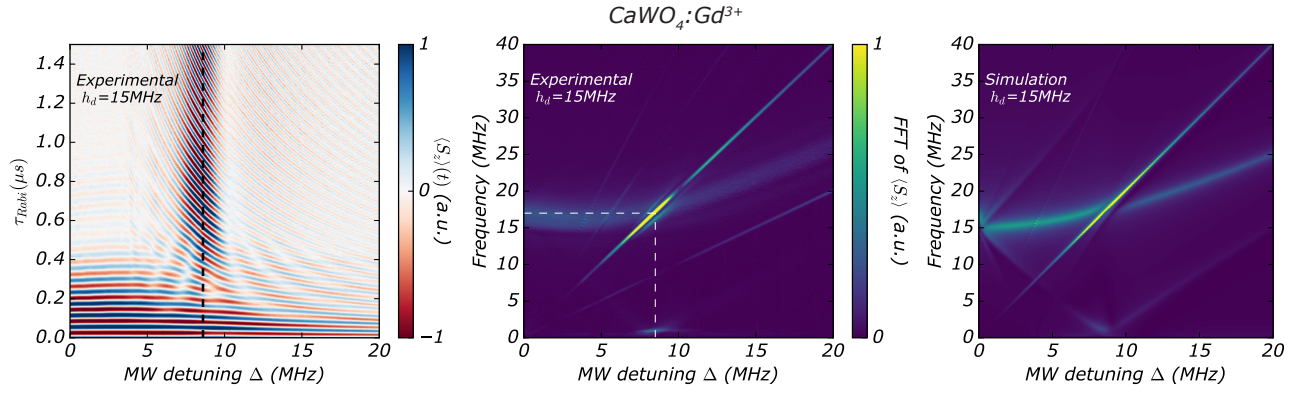


Figure 3. **Rabi dynamics as a function of detuning at fixed drive level  $h_d$ .** **a**, Contour plot showing  $S_z$  as a function of pulse length  $\tau_{Rabi}$  and microwave detuning  $\Delta$ . At  $F_R = 2\Delta$  (dashed), the Rabi oscillations are optimally sustained by the image pulse. **b**, The FFT of **a** shows an intense peak where the optimum imaging is achieved (dashed). **c**, A simulated FFT using the rotating wave approximation with the parameters of **b**, is in agreement with the experimental observations.

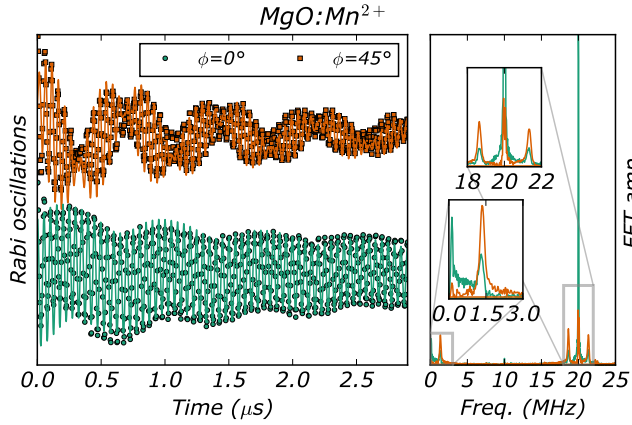


Figure 4. **Phase-tunable Floquet dynamics.** Rabi oscillations of  $Mn^{2+}$  at 40 K for two values of  $\phi$ . For  $\phi = 0^\circ$  (green symbols), the drive and the image pulses have the same initial phases resulting in optimally sustained Rabi oscillation. For  $\phi = 45^\circ$  (orange symbols), the spin torques generated by the two pulses induce strong beatings in the spin dynamics ( $h_{d,i}$  terms of  $\mathcal{H}_{RF}$  are  $\perp$ ). The plain lines are simulations using our model with no fit parameters. The right panel shows the two experimental FFT traces. The green one has a well-defined peak at  $F_R$  while in the other one the beatings (top inset) are separated by twice the Floquet mode frequency (bottom inset).

*Supplementary Information* for more information). Since the effect of the image is the central part of this paper, we have characterized the AWG bridge using a spectrum analyzer, right before the power amplification stage. An example of spectrum is presented in Fig. S5 of the *Supplementary Information*. The power of the image  $f_0 - \Delta$  is lower by  $\approx -18$  dB than  $f_0 + \Delta$ . Consequently, an amplitude ratio of the MW magnetic fields  $h_i/h_d$  around  $\sim 0.12$  is used in simulations.

*Pulse sequence.* First, the system is set to be in reso-

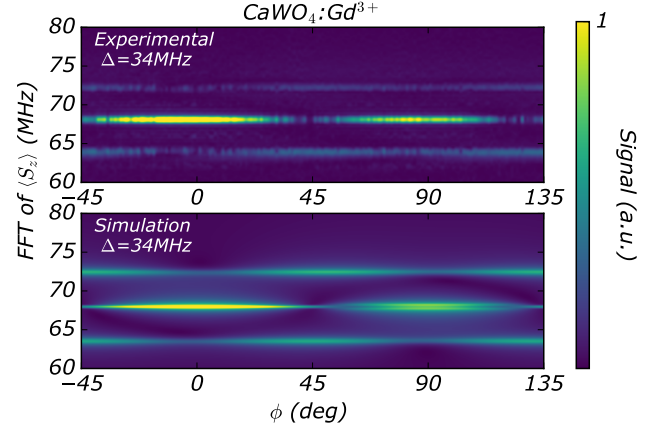


Figure 5. **Phase-dependence of the Floquet mode.** Experimental (top) and simulated (bottom) FFT of Rabi oscillations for  $\Delta = h_d/\sqrt{3} = 34$  MHz as a function of  $\phi$  (amplitude is normalized to the highest peak). For  $\phi = 2k\pi/4, k \in \mathbb{N}$ , Rabi oscillations have a single mode  $F_R$  while for  $\phi = (2k+1)\pi/4$  a splitting of twice the Floquet mode frequency is observed. While its frequency is fixed, the intensity of the Floquet mode changes gradually, with a period of  $\pi/2$ .

nance condition  $g\mu_B H_0 = hf_0$ . The drive pulse of amplitude  $h_D$ , frequency  $f_0 + \Delta$  and length  $\tau_{Rabi}$  induces Rabi oscillation in detuning regime. At the same moment the image pulse (generated through the IQ mixer) of amplitude  $h_I$ , frequency  $f_0 - \Delta$  and the same length  $\tau_{Rabi}$  also irradiate the spins. In order to probe  $\langle S_z(\tau_{Rabi}) \rangle$  at the end of the Rabi sequence, we wait a time longer than  $T_2$ , such that  $\langle S_x \rangle \approx \langle S_y \rangle \approx 0$ , followed by  $\pi/2 - \pi$  pulses to create a Hahn echo of intensity proportional to  $\langle S_z \rangle$ .

*Spin systems.* The methodology presented here is demonstrated on different spin systems: the nitrogen substitution in diamond P1 defect ( $S = 1/2$ ) (concentration :100 ppm),  $Mn^{2+}$  impurities in MgO ( $S = 5/2$ ) with a concentration of 10 ppm and  $Gd^{3+}$  impurities in

CaWO<sub>4</sub> ( $S = 7/2$ ) with a concentration of 50 ppm. Despite the large Hilbert space of the Mn<sup>2+</sup> and Gd<sup>3+</sup> spin Hamiltonians, the orientation of the magnetic field and the frequency and power of the microwave excitation are chosen to avoid multiple level transitions and thus select only one resonance<sup>19</sup>. Therefore, the spin systems can be considered as effective two-level systems undergoing coherent Rabi rotations. The spin Hamiltonians, operating parameters (fields and frequencies) as well as characteristic  $T_{1,2}$  times for these materials are given in the Supplementary Information.

*Simulation explanation.* In the rotating frame, the Hamiltonian describing the dynamics of the electron spin is given by Eq. S14 in the *Supplementary Information*:  $\mathcal{H}_{RF} = -\Delta S_z + S_+ [h_d e^{-i(\phi - \pi/2)} + h_i e^{i(4\pi\Delta t + \phi + \theta + \pi/2)}]$ . When the "image" pulse is not applied, the Hamiltonian is time independent and the propagator is simply the matrix exponential of the Hamiltonian:  $U_p(t) = \exp(-i2\pi\mathcal{H}_{RF}t)$ . When the image pulse is present ( $h_i > 0$ ), the Hamiltonian becomes explicitly time-dependent. Although a second canonical transformation RWA could remove the time dependence if  $\Delta \gg h_i$ , it is impor-

tant to leave  $\Delta$  as a free parameter since the methods works at resonance as well ( $\Delta = 0$ ). Thus, for the sake of generality, we solved numerically the explicit time-dependent differential equations using the quantum toolbox QuTIP<sup>20</sup>. The parameters used in the simulation have been measured independently: the microwave drive field  $h_d$  has been calibrated using the frequency of Rabi oscillations at no detuning ( $\Delta = 0$ ), the image drive  $h_i$  was measured by a spectrum analyzer directly connected to the output of the AWG, relaxation ( $T_1$ ) and decoherence ( $T_2$ ) times were measured by inversion recovery and Carr-Purcell-Meiboom-Gill (CPMG) protocol, respectively (see *Supplementary Information, Sect I*).

## DATA AVAILABILITY

Data sets generated and analyzed during the current study are available from the corresponding author on request.

\* sylvain.bertaina@im2np.fr

† ic@magnet.fsu.edu

<sup>1</sup> Chirolli, L. & Burkard, G. Decoherence in solid-state qubits. *Advances in Physics* **57**, 225–285 (2008).

<sup>2</sup> Yoneda, J. *et al.* A quantum-dot spin qubit with coherence limited by charge noise and fidelity higher than 99.9%. *Nat. Nanotechnol.* **13**, 102–106 (2018).

<sup>3</sup> Viola, L. & Lloyd, S. Dynamical suppression of decoherence in two-state quantum systems. *Phys. Rev. A* **58**, 2733–2744 (1998).

<sup>4</sup> Viola, L., Knill, E. & Lloyd, S. Dynamical Decoupling of Open Quantum Systems. *Phys. Rev. Lett.* **82**, 2417–2421 (1999).

<sup>5</sup> Cai, J.-M. *et al.* Robust dynamical decoupling with concatenated continuous driving. *New J. Phys.* **14**, 113023 (2012).

<sup>6</sup> Farfurnik, D. *et al.* Experimental realization of time-dependent phase-modulated continuous dynamical decoupling. *Phys. Rev. A* **96**, 013850 (2017).

<sup>7</sup> Teissier, J., Barfuss, A. & Maletinsky, P. Hybrid continuous dynamical decoupling: A photon-phonon doubly dressed spin. *J. Opt.* **19**, 044003 (2017).

<sup>8</sup> Rohr, S. *et al.* Synchronizing the Dynamics of a Single Nitrogen Vacancy Spin Qubit on a Parametrically Coupled Radio-Frequency Field through Microwave Dressing. *Phys. Rev. Lett.* **112**, 010502 (2014).

<sup>9</sup> Facchi, P., Lidar, D. A. & Pascazio, S. Unification of dynamical decoupling and the quantum Zeno effect. *Phys. Rev. A* **69**, 032314 (2004).

<sup>10</sup> Fanchini, F. F., Hornos, J. E. M. & Napolitano, R. d. J. Continuously decoupling single-qubit operations from a perturbing thermal bath of scalar bosons. *Phys. Rev. A* **75**, 022329 (2007).

<sup>11</sup> Shu, Z. *et al.* Observation of Floquet Raman Transition in a Driven Solid-State Spin System. *Phys. Rev. Lett.* **121**,

210501 (2018).

<sup>12</sup> Saiko, A. P., Markevich, S. A. & Fedaruk, R. Multiphoton Raman transitions and Rabi oscillations in driven spin systems. *Phys. Rev. A* **98**, 043814 (2018).

<sup>13</sup> Yu, M. *et al.* Experimental measurement of the complete quantum geometry of a solid-state spin system. *ArXiv181112840 Cond-Mat Physicsquant-Ph* (2018). 1811.12840.

<sup>14</sup> Russomanno, A. & Santoro, G. E. Floquet resonances close to the adiabatic limit and the effect of dissipation. *J. Stat. Mech. Theory Exp.* **2017**, 103104 (2017).

<sup>15</sup> Bienfait, A. *et al.* Controlling spin relaxation with a cavity. *Nature* **531**, 74–77 (2016).

<sup>16</sup> Yue, G. *et al.* Sensitive spin detection using an on-chip SQUID-waveguide resonator. *Appl. Phys. Lett.* **111**, 202601 (2017).

<sup>17</sup> Probst, S. *et al.* Inductive-detection electron-spin resonance spectroscopy with 65 spins/ Hz sensitivity. *Appl. Phys. Lett.* **111**, 202604 (2017).

<sup>18</sup> Toida, H. *et al.* Electron paramagnetic resonance spectroscopy using a single artificial atom. *Commun Phys* **2**, 1–7 (2019).

<sup>19</sup> Bertaina, S. *et al.* Multiphoton Coherent Manipulation in Large-Spin Qubits. *Phys. Rev. Lett.* **102**, 50501–50504 (2009).

<sup>20</sup> Johansson, J., Nation, P. & Nori, F. QuTiP 2: A Python framework for the dynamics of open quantum systems. *Comput. Phys. Commun.* **184**, 1234–1240 (2013).

## ACKNOWLEDGEMENTS

ESR measurements were supported by the CNRS research infrastructure RENARD (award number IR-RPE CNRS 3443). Partial support by the National Science

Foundation Cooperative Agreement No. DMR-1644779 and the State of Florida is acknowledged.

surements were performed at Lille University by H.V. and S.B.. All authors contributed to the writing of the manuscript.

#### **AUTHOR CONTRIBUTIONS**

S.B. and I.C. designed the experiment, analyzed the data and provided the theoretical background. Mea-

#### **COMPETING INTERESTS**

the Authors declare no Competing Financial or Non-Financial Interests